UNIVERSITY OF CALIFORNIA SAN DIEGO

Combining Land and Lake Bottom Magnetotelluric Measurements to Study Volcanic Systems in Mono Basin, California

A thesis submitted in partial satisfaction of the
requirements for the degree Master of Science

in

Earth Sciences

by

Hannah Camille Peterson

Committee in charge:

Steven Constable, Chair
Geoffrey Cook
Gabi Laske

2020

This thesis of Hannah Camille Peterson is approved, and it is acceptable in quality and form for publication on microfilm and electronically:

_____

_____

_____

Chair

University of California San Diego

2020

DEDICATION

To my parents.

Contents

List of Figures

List of Tables

ACKNOWLEDGEMENTS

There were many people who made my two years at Scripps an enriching, challenging and exciting experience. First, thank you to Steve Constable for his time and efforts in advising me. He allowed me to work and think independently while also giving me valuable research guidance and development as a scientist. I would like to acknowledge Geoff Cook and Gabi Laske for agreeing to sit on my committee, taking their time to learn about my project and providing their help with anything along the way. Next I'd like to thank Jared Peacock at the USGS for his assistance in the data collection and processing for this project. Jared was always available and happy to answer questions about the data, instruments, and geologic context. He also helped greatly with 3D modeling and inversion of the data. Thank you to Pieter Share for tirelessly helping me with many of the problems and questions I ran into and for working with me on the data reformatting and inversions. I'd also like to acknowledge Peter Kanneberg and Shunguo Wang for always being happy to answer my questions and give input on my work. Thank you to the Marine EM lab and the 2018 IGPP cohort for providing great company, laughs, homework help and support. Finally, thank you to my family for their continued support throughout my graduate studies.

ABSTRACT OF THE THESIS

Combining Land and Lake Bottom Magnetotelluric Measurements to Study Volcanic Systems in Mono Basin, California

by

Hannah Camille Peterson

Master of Science in Earth Sciences, 2020

Professor Steven Constable, Chair

In volcanic settings, magnetotelluric methods can be a useful tool for geophysical investigation because the host rock is typically resistive while in contrast the features of interest, such as fluids and heat sources, will be electrically conductive. The work presented in this thesis are findings from magnetotelluric data taken in Mono Basin, California to study volcanic systems in the area and give suggestions for future eruption potential. The Long Valley volcanic region and Mammoth Mountain area have experienced heightened geologic unrest in the recent decades with ground deformation, earthquake swarms and CO_2 emissions, which are an indication of an ongoing volcanic threat.

Since Long Valley Caldera's formation 0.76 Ma, there has been a north-trending cycle of eruptions creating the Inyo-Mono Crater chain likely due to extensional

tectonics. The most recent event occurred less than 350 years ago in Mono Lake, creating Paoha Island. Previous geophysical investigations of this area have identified conductive anomalies in Mono Basin that suggest fluid flow and heat sources. Mono Lake previously served as an equivocal gap in the data set, motivating a field campaign using modified seafloor EM receivers. Following lake deployments, several land stations were deployed north of the lake for further investigation. 2D inversions of the data show a large conductive body that underlies a smaller anomaly 2-5 km under Mono Lake. Guided by existing geologic observations, this system is interpreted to be a magma chamber or hydrothermal reservoir that underlies hot fluids with a local fault facilitating fluid and heat flow between the two bodies. The interpretation of the shallow section is supported with observations of hot springs at the surface. The melt fraction of the larger, deep conductor is estimated in a range of 5 - 40%. The anomaly extends to the north of Mono Lake past the limits of the data set, suggesting that another eruption is likely following the northward trend.

Additionally, a process for using lake-bottom MT measurements in 3D inversion is presented in this work. Bathymetry cannot be included in 3D models using the ModEM code but the measurements collected on the lake bottom can be upward continued to the surface using the 1D MT recursion relation. Using these modified data, the 3D inversion is in good agreement with the 2D inversion and shows a deep conductive feature that funnels upwards to a shallower conductor directly beneath Mono Lake.

Chapter 1

Introduction

1.1 Motivation

The onset of geologic unrest during the last four decades in Long Valley has sparked concern for safety of the residents and tourists that visit the popular surrounding areas such as Mammoth Lakes. The most notable manifestation has been underground seeps of CO_2 gas, particularly around Mammoth Mountain, that is responsible for killing trees in the area and can be a threat to humans. With an extensive history of volcanism in this area, this may indicate that magma is moving to shallower depths in the crust. Earthquake swarms and surface deformation have also occurred in the last 40 years, motivating many scientific studies using geologic observations, geophysics and geochemistry. Characterizing the subsurface structure and its constituents leads to a broader understanding of the potential volcanic hazard and can be used for mitigation and future planning. This study is a continuation of the geophysical investigations carried out by the United States Geological Survey (USGS) by using electromagnetic data collected in Mono Basin to create models of the subsurface. Geologic interpretation of these models may help to characterize the nature of the Long Valley magma body and its associated hydrothermal system and aid in any eruption forecasting undertaken in the future. Further aspects for this work compares the use of multi-station magnetotelluric processing with conventional processing methods, as well as developing a process for using lake-bottom data in 3D modeling codes that cannot include bathymetry.

1.2 Geologic Background

1.2.1 Tectonic Setting

The Owens Valley is a graben that is found between the Great Basin to the east and the Sierra Nevada fault to the west. Repeated episodes of strike-slip earthquakes during the late Miocene to beginning of the Pleistocene in this region led to the uplift of the Sierra Nevada and White Mountain escarpments, simultaneously forming the downdropped block that is now Owens Valley [Pakiser et al., 1964]. The Owens Valley region is home to Long Valley Caldera, Mono Basin and slopes of the surrounding mountain ranges (Sierra Nevada, White and Inyo). The "Basin and Range" topography allowed the intrusion of northwest-striking dike in the basin and fed the volcanism in Long Valley and Mono Basin [Nixon, 2012]. "Basin and Range" is the result of extensional tectonics, causing crustal thinning and allowing the upwelling of magma from the mantle. Gravitational surveys done by Gilbert et al. [1968] suggests that the structure of Mono Basin, a volcanic-tectonic depression, has been influenced by volcanism and deformation simultaneously since the Pliocene.

1.2.2 Long Valley Caldera

The Long Valley Caldera is one of three well-known Quaternary, silicic calderas in the western United States, along with the Valles in New Mexico and Yellowstone in Wyoming. Long Valley Caldera formed in response to a supereruption (0.76 Ma) that deposited 600 km^3 of pyroclastic outflow units locally (the Bishop Tuff) and deposited pyroclastic fall across the western U.S. as far as Nebraska (see Figure 1.1). Since this eruption, resurgent activity, including regional tumescence and dome-building eruptions, has occurred in the caldera due to magmatic uplift. During the late Pleistocene the

Owens River cut through the Bishop Tuff in the Owens Valley to form the Owens River Gorge. Today, the caldera is host to an active hydrothermal system, including hot springs and fumaroles [Peacock et al., 2015].

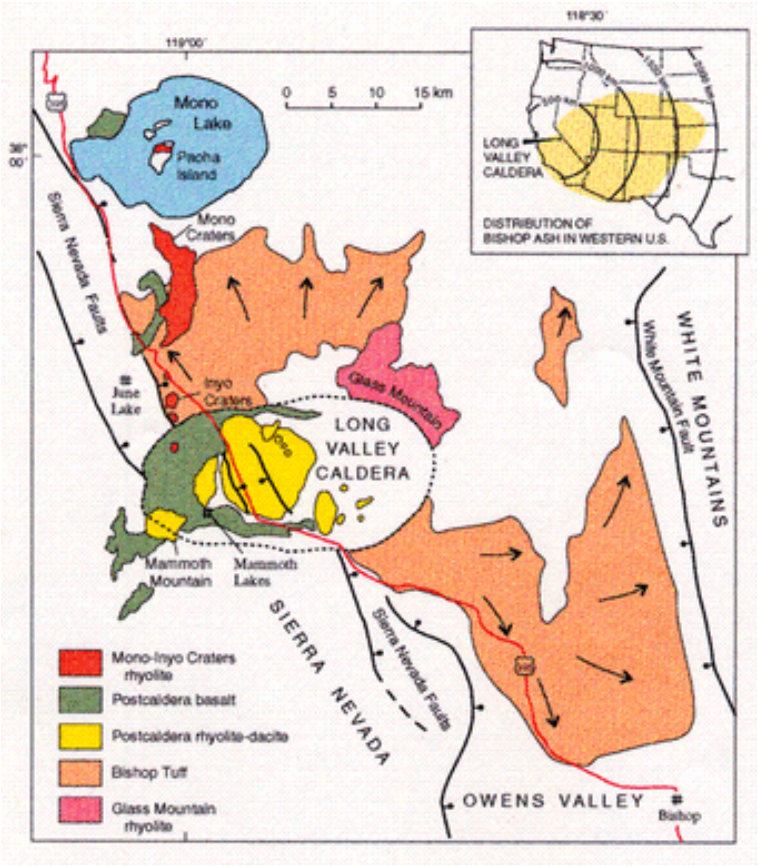

Figure 1.1: Geologic composition of Long Valley and Mono Basin areas, with the extent of the Bishop Tuff fall deposits shown in the top right. The Long Valley caldera is composed mostly of rhyolite-dacite, while the Mono-Inyo craters are rhyolite. Figure courtesy USGS.

1.2.3 Inyo-Mono Crater Chain

Following the 0.76 Ma Bishop Tuff eruption there have since been more than 30 eruptions that resulted in the formation of Inyo-Mono Crater chain, which begins just south of Mammoth Mountain and extends 45 km northwards towards Mono Basin [Bailey, 1989a]. Most of these volcanic craters are exposed rhyolitic lava domes and flows

erupted during the late Pleistocene to Holocene from now-buried volcanic vents. Figure 1.2 shows the Mono-Inyo craters in relation to Long Valley and the towns of Mammoth Lakes and Lee Vining. The youngest of these features is Paoha Island sitting in Mono Lake, which erupted 350 years ago as an extrusion of andesitic lava associated with a shallow intrusion that uplifted lacustrine sediments. The eruption was relatively small in volume in comparison to past eruptions [Bursik and Sieh, 1986]. Table 1.1 lists the major eruptions that occurred during the Holocene.

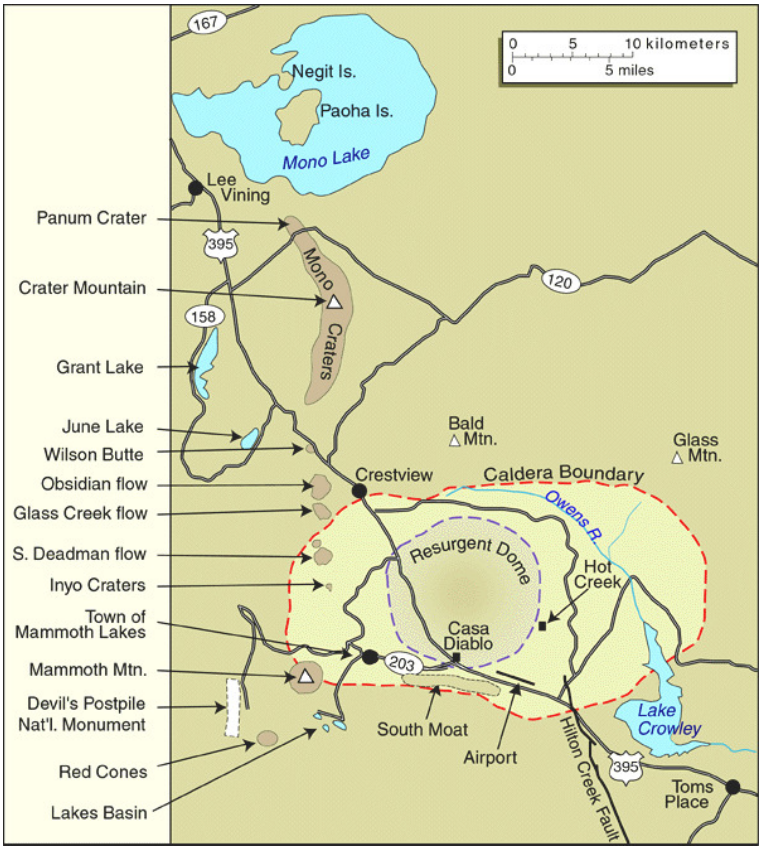

Figure 1.2: Map recreated from Bailey [1989b] of the Mono-Inyo Crater chain, showing major highways and towns, lakes, and regional faults. Figure courtesy USGS.

Table 1.1: List of Holocene-age eruptions for the Inyo-Mono Crater chain.

Start Date	**Evidence**	**Activity Area**
1380 ± 50 years	Radiocarbon	Inyo Craters (S Deadman, Obsidian, Glass Creek)
1350 ± 20 years	Dendrochronology	Mono Craters (Panum Crater)
1000 ± 200 years	Hydration Rind	Mono Craters (NW edge of NW Coulee)
0620 ± 27 years	Radiocarbon	Southern Mono Craters (South Coulee area)
0490 ± 100 years	Radiocarbon	Mono Craters (Pumice Pit dome)
0440 ± 100 years	Radiocarbon	Southern Mono Craters
0320 ± 200 years	Radiocarbon	Mono Craters (South Coulee)
0290 ± 50 years	Radiocarbon	Inyo Craters (Wilson Butte)
0010 ± 200 years	Radiocarbon	Mono Craters (South Coulee)
0700 BCE ± 800 years	Hydration Rind	Central Mono Craters
3850 BCE ± 1160 years	Hydration Rind	Mono Craters (N of Punchbowl)
4050 BCE	Hydration Rind	Inyo Craters (N of Deadman Creek)
6750 BCE± 1740 years	Hydration Rind	Mono Craters (Punchbowl)

1.3 Previous Work

The United States Geologic Survey (USGS) has done extensive work in imaging the complex subsurface structure in Long Valley and Mono Basin. It has deployed several MT stations in the southeastern part of Mono Basin and modeled the data in 3D to characterize features associated with the magma body, including partial melt zones, cold plutons and regional fault structure [Peacock et al., 2015].

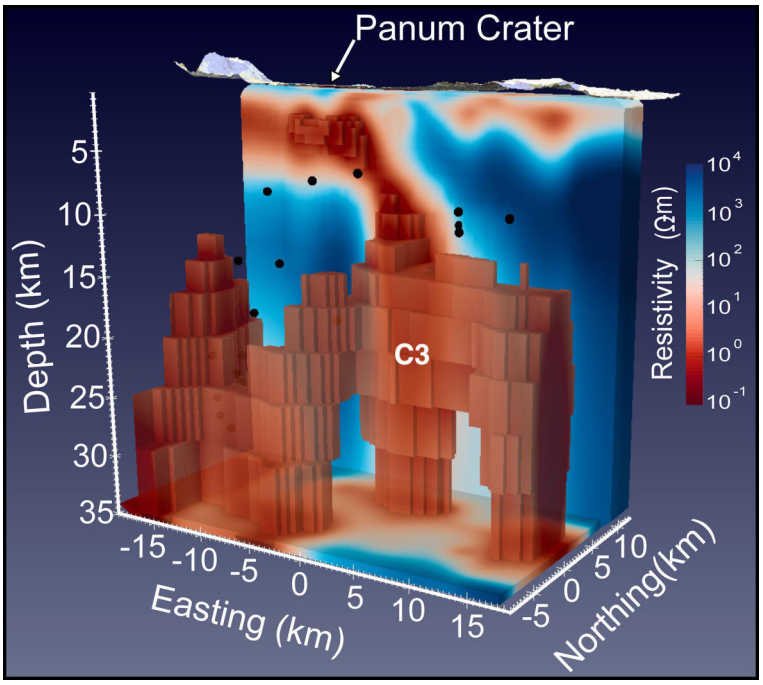

Figure 1.3: 3D model of Mono Basin from Peacock et al. [2015] showing large conductive anomalies at around 10 km depth. Shallower conductive sources are located below the vents of the Panum crater, which is south of Mono Lake.

3D modeling shows large conductive bodies that are near-vertical at around 10 km depth that have been interpreted as magmatic melt zones; these have been attributed as source material for past eruptions. These conductors are in good agreement with previous geophysical observations. The **C3** conductor labeled in Figure 1.3 is possibly magmatic and connects to shallower conductive structure just under the Panum Crater that is interpreted as hydrothermal fluids. As shown in Figure 1.2, the Panum Crater lies just to the south of Mono Lake, and was the northern limit of the previous USGS MT data set. The significant findings of this study motivated our data collection in Mono Lake, as described in Section 2.2.

Chapter 2

Theory and Methods

The work presented in this thesis uses geophysical electromagnetic methods for the investigation of Mono Lake and the surrounding area. This chapter discusses the theory of electrical methods in geophysics, followed by an explanation of the data collection and processing, as well as the the modeling approach and inversion.

2.1 Electromagnetic Methods

Electrical resistivity, when measured in the Earth's subsurface, can unveil important information about the rock properties and structures at depth. In the Earth, the electrical resistivty ranges over multiple orders of magnitude, up to 11 orders, making it an effective way to determine what structures are under the surface. Figure 2.1 shows typical resistivities of Earth materials.

Electrical resistivity is a particularly useful measurement when studying volcanic settings because the host rock is typically resistive, around 100 Ω-m or more, while the targets are electrically conductive, such as fluids and heat sources. Resistivity values are recovered through electromagnetic measurements in the field, which use electric and magnetic field variations to examine the electrical signature of subsurface layers and features. These measurements can be carried out passively, using natural variations in the fields, or actively using an induced energy source to measure the response.

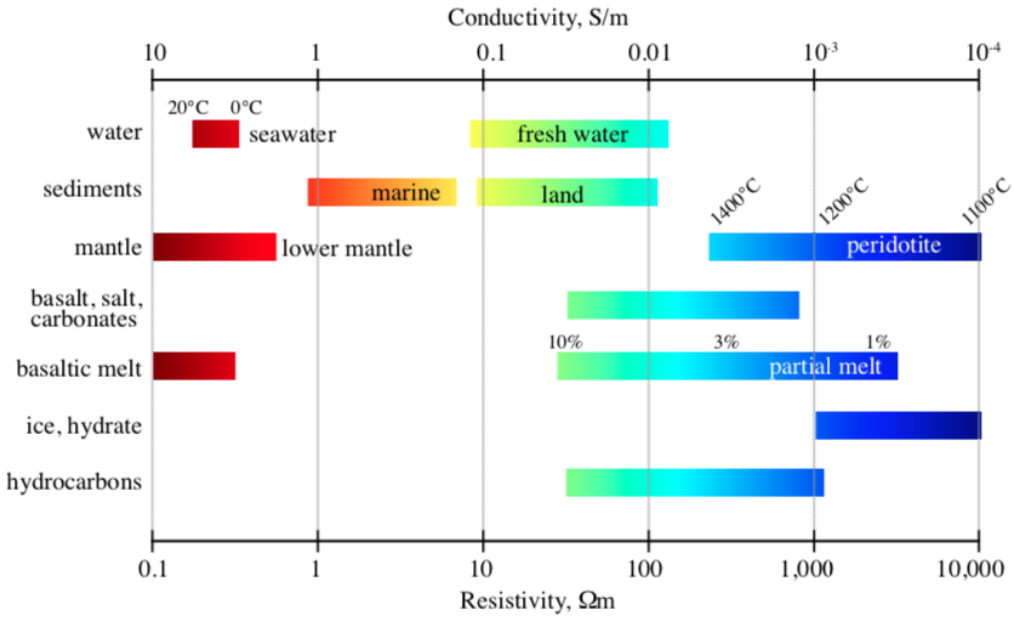

Figure 2.1: A spectrum of electrical resistivities ranging over five orders of magnitude for different Earth materials. Figure courtesy Steven Constable.

Electromagnetic fields are described by Maxwell's Equations, which relate the magnetic and electric fields in time. We begin with the following Maxwell's equations.

$$\nabla \times \mathbf{E} = -\frac{\delta \mathbf{B}}{\delta t} \tag{2.1}$$

$$\nabla \times \mathbf{B} = \mu_o \mathbf{J} \tag{2.2}$$

where $\mathbf{E}$ is the free electric field (V m^{-1}), $\mathbf{J}$ is the current density (A m^{-2}), and $\mathbf{B}$ is the magnetic flux density (T). To describe the electromagnetic properties of matter, the conductivity (σ), permittivity (ϵ) and (μ) are used in the following constitutive relations. These equations apply assuming a homogeneous isotropic medium.

$$J = \sigma \mathbf{E} \tag{2.3}$$

In order to describe the electric and magnetic fields as a function of frequency, Equation

2.3 (Ohm's Law) is substituted into Equation 2.2 (Ampere's Law) to yield $\nabla \times \mathbf{B} = \mu_o \sigma \mathbf{E}$. The curl of both sides is

$$\nabla \times \nabla \times \mathbf{B} = \mu_o \sigma \nabla \times \mathbf{E}$$

Equation 2.1 can be substituted for $\nabla \times \mathbf{E}$ and use the vector identity ($\nabla \times \nabla \times \mathbf{A} = \nabla(\nabla \cdot \mathbf{A} - \nabla^2 \mathbf{A})$.

$$\nabla(\nabla \cdot \mathbf{B}) - \nabla^2 \mathbf{B} = -\mu_o \sigma \frac{\delta \mathbf{B}}{\delta t}$$

Gauss' Law states that there are no monopoles allowed in magnetism ($\nabla \cdot \mathbf{B} = 0$), so we can reduce the equation to

$$\nabla^2 \mathbf{B} = \mu_o \sigma \frac{\delta B}{\delta t} \tag{2.4}$$

In a similar fashion, the curl of Faraday's Law and yields

$$\nabla \times \nabla \times \mathbf{E} = -\frac{\delta}{\delta t}(\nabla \times \mathbf{B})$$

and substituting Equation 2.2 and Equation 2.3 the result is

$$\nabla \times \nabla \times \mathbf{E} = -\mu_o \sigma \frac{\delta \mathbf{E}}{\delta t}$$

Taking the divergence of both sides of Equation 2.2 and using another vector identity ($\nabla \cdot (\nabla \times \mathbf{A})$ we get $\nabla \cdot \mathbf{J} = 0$. For the halfspace case it is assumed that the conductivity is constant, so the divergence of the electric field is $\nabla \cdot E = 0$. The result is a similar equation to Equation 2.4.

$$\nabla^2 \mathbf{E} = \mu_o \sigma_o \frac{\delta E}{\delta t} \tag{2.5}$$

Equations 2.4 and 2.5 are the diffusion equations that describe the behaviour of the electric and magnetic field. Because the MT method is dependent upon frequency and wavelength, these equations must be described in the frequency domiain. Using the time

dependence relation for **B** and **E**, $e^{i\omega t}$, where ω is the angular frequency, equal to $2\pi f$, the fields are described at a single frequency.

$$\mathbf{B}(t) = \mathbf{B}e^{i\omega t} \qquad \frac{\delta \mathbf{B}}{\delta t} = i\omega \mathbf{B}$$
$$\mathbf{E}(t) = \mathbf{E}e^{i\omega t} \qquad \frac{\delta \mathbf{E}}{\delta t} = i\omega \mathbf{E}$$

Substituting the latter two relations for **B** and **E** into the diffusion equations the result is

$$\nabla^2 \mathbf{E} = i\omega \mu_o \sigma o \mathbf{E}$$
$$\nabla^2 \mathbf{B} = i\omega \mu_o \sigma o \mathbf{B}$$

Under the assumption that B is a purely horizontal and uniform field dependent upon frequency ω, **B** can only vary with depth z. Using the definition of the Laplacian and defining a complex wavenumber $k = \sqrt{i\omega\mu_o\sigma_o}$, where σ_o is the value for a uniform halfspace, the diffusion equations become

$$\frac{d^2 B}{dz^2} = k^2 B(z) \tag{2.6}$$

which is a second order linear differential equation with the solution $B(z) = c_1 e^{kz} + c_2 e^{-kz}$. The constant c_1 is zero because the first term increases as depth z increases. At the surface, z=0, thus $c_2 = B_o e^{i\omega t}$ and the complex wavenumber can be rewritten as follows.

$$k = \sqrt{i\omega\mu_o\sigma_o} = (1+i)\sqrt{\frac{\omega\mu_o\sigma_o}{2}} = \frac{(1+i)}{z_o} \tag{2.7}$$

where $z_o = \sqrt{\frac{2}{\omega\mu_o\sigma o}}$. The electromagnetic signal attenuates with depth, and the behavior is described by this term, called the skin depth z_o. The value of the skin depth describes the decay of the signal to $1/e$ or about 37% of the original [Spies, 1989]. Rewritten in more commonly used terms resistivity (ρ) and frequency (f), the skin depth becomes

$$z_s \approx 500\sqrt{\rho/f} \tag{2.8}$$

Skin depth calculations determine what depth of penetration can be obtained at a given frequency, which is important for survey planning and interpretation of data. As the relation shows, a higher frequency leads to shallower skin depths, and lower frequencies penetrate deeper.

2.1.1 The Magnetotelluric Method

As described by Cagniard [1953], the magnetotelluric (MT) method is used to recover electrical resistivity through measurement of Earth's naturally occurring electric and magnetic fields, initially proposed for oil and mineral prospecting. The MT source field arises from the interactions between solar winds and the Earth's magnetosphere, generating lower frequency energy, at values less than about 1 Hz. Frequencies higher than 1 Hz are generated by worldwide thunderstorms and lightning strikes. Starting again by substituting Equation 2.3 (Ohm's Law) into Equation 2.2, the curl of the magnetic field $\nabla \times \mathbf{B}$ is equal to $\mu_o \sigma \mathbf{E}$. In order to take the curl of B, the following definition is used.

$$\nabla \times \mathbf{A} = (\tfrac{\delta A_z}{\delta y} - \tfrac{\delta A_y}{\delta z}, \tfrac{\delta A_x}{\delta z} - \tfrac{\delta A_z}{\delta x}, \tfrac{\delta A_y}{\delta x} - \tfrac{\delta A_x}{\delta y})$$

Assuming that the magnetic field is uniform in the y-direction, the horizontal field in the x-direction is derived and leaves only the term $\frac{\delta B_x}{\delta z}$.

$$\frac{dB_x}{dz} = \mu_o \sigma_o E_y \quad or \quad E_y = \frac{1}{\mu_o \sigma_o} \frac{dB_x}{dz} \tag{2.9}$$

Solving for the differential equation and substituting in the value for k from Equation 2.7, the diffusion equation above becomes

$$B(z) = B_o e^{i\omega t} B^{-(1+i)z/z_o} \tag{2.10}$$

The derivative of the magnetic field **B** is calculated in respect to x, yielding $\frac{dB_x}{dz} = \frac{1+i}{z_o} B_x$ and substituted into Equation 2.9.

$$E_y = \frac{1+i}{\mu_o \sigma_o z_o} B_x = -\frac{k}{\mu_o \sigma_o} B_y \tag{2.11}$$

Using Equation 2.11, the resistivity of a halfspace can be described by taking the ratio of magnetic and electric fields.

$$\left|\frac{E}{B}\right|^2 = \left(\frac{k}{\mu_o \sigma_o}\right)^2 = \left(\frac{\sqrt{i\omega\mu_o\sigma_o}}{\mu_o\sigma_o}\right)^2 = \frac{\omega}{\mu_o\sigma_o} \tag{2.12}$$

$$\rho = \frac{\mu_o}{\omega}\left|\frac{E}{B}\right|^2 \tag{2.13}$$

In an MT survey, the magnetic and electric fields are recorded in up to five components, E_x, E_y, E_z, B_x and B_z. The ratio of the magnetic and electric fields is often referred to at the electrical impedance Z and can be calculated for the 2D case using the impedance tensor.

$$\begin{pmatrix} E_x \\ E_y \end{pmatrix} = \begin{pmatrix} Z_{xx} & Z_{xy} \\ Z_{yx} & Z_{yy} \end{pmatrix} \begin{pmatrix} B_x \\ B_y \end{pmatrix} \tag{2.14}$$

$$\mathbf{E} = \mathbf{ZB} \qquad \mathbf{Z} = \mathbf{E/B} \tag{2.15}$$

In the 2D case, the diagonal impedances Z_{xx} and Z_{yy} will equal 0 if the x or y axis is along the direction of strike. The off-diagonal impedances are separated into two modes, transverse electric (TE) and transverse magnetic (TM). For TE mode, $Z_{xy} = E_x/B_y$, the electric field orientation is along the line of strike and the magnetic field is perpendicular. The opposite case is the TM mode $Z_{yx} = E_y/B_x$. Due to their orientations each mode has a differing sensitivity to a conductive structure.

In the case where the subsurface structure is horizontally layered and varying with depth (z-direction), the impedance can be modeled in one-dimension using a recursion relation that includes information about each layer. Ward and Hohmann [1988] described this using a transfer function that relates the impedance $\hat{Z}_n$ at the top of a layer n with thickness h_n in terms of the impedance at the top of the layer below it, counting downwards.

$$\hat{Z}_n = Z_n \frac{\hat{Z}_{n+1} + Z_n tanh(ik_n h_n)}{Z_n + \hat{Z}_{n+1} tanh(ik_n h_n)} \tag{2.16}$$

where Z_n is the intrinstic impedance and is equal to $\omega\mu/k_n$. For this layered Earth model, the bottom layer is bound by an infinite halfspace, so $h_{N+1} = \infty$, which makes the term $tanh(ik_{N+1}h_{N+1})$ equal to 1. In this case, Equation 2.16 becomes

$$\hat{Z}_{N+1} = Z_N = \frac{\omega\mu}{k_N}$$

As previously defined, the complex wavenumber k is equal to $\sqrt{i\omega\mu_o\sigma_o}$. So, using known conductivities of a layered Earth, one can model the impedance response at any layer. Equations 2.17 and 2.18 yield apparent resistivity and phase in terms of Z. The apparent resistivity as a function of frequency and phase differences are diagnostic of the true resistivities of each layer [Cagniard, 1953].

$$\rho_a = \frac{1}{\omega\mu_o}\left|\frac{E_x}{B_y}\right|^2 \tag{2.17}$$

$$\phi = tan^{-1}\left(\frac{E_x}{B_y}\right) \tag{2.18}$$

2.2 Data Collection and Instrumentation

In 2017, Scripps and USGS scientists collected MT data in Mono Lake using a modified version of the Scripps seafloor EM receiver, typically only used in marine

settings. A few modifications allowed these autonomous logging systems to be used in the lake bottom, which is only about 42 meters at its deepest point as shown in the bathymetry map in Figure 2.3. The instruments were moored, so acoustic and flotation systems were removed, and the electric dipoles are shortened from ten to three meters. Seven receivers were deployed at a time and left in the lake bed for 48 hours. They were recovered and moved twice for a total of 21 sites. The station locations are shown in Figure 2.3. The systems can record up to 8 channels of 24-bit data. Induction coil magnetometers were used as a remote reference south of the lake, continuously recording during the entire survey.

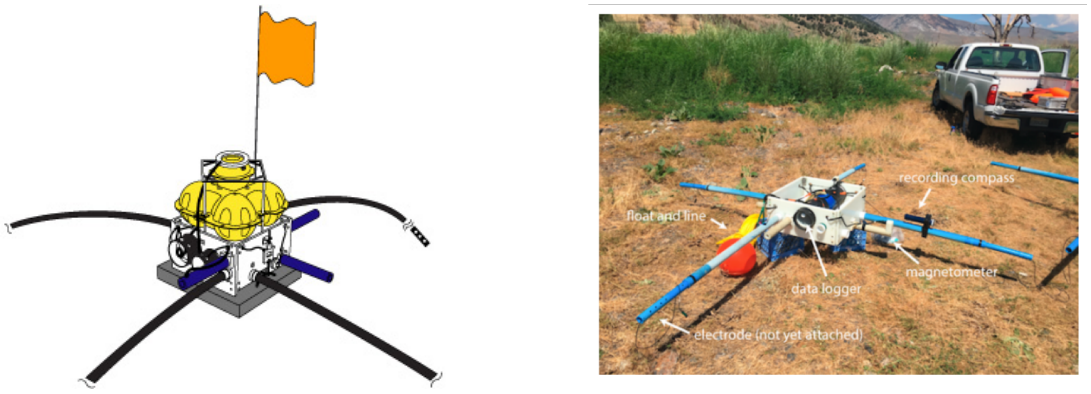

(a) **(b)**

Figure 2.2: (a) Schematic of a Scripps EM reciever, typically used in a marine setting. (b) The modified version of the marine receiver used in Mono Lake in 2017.

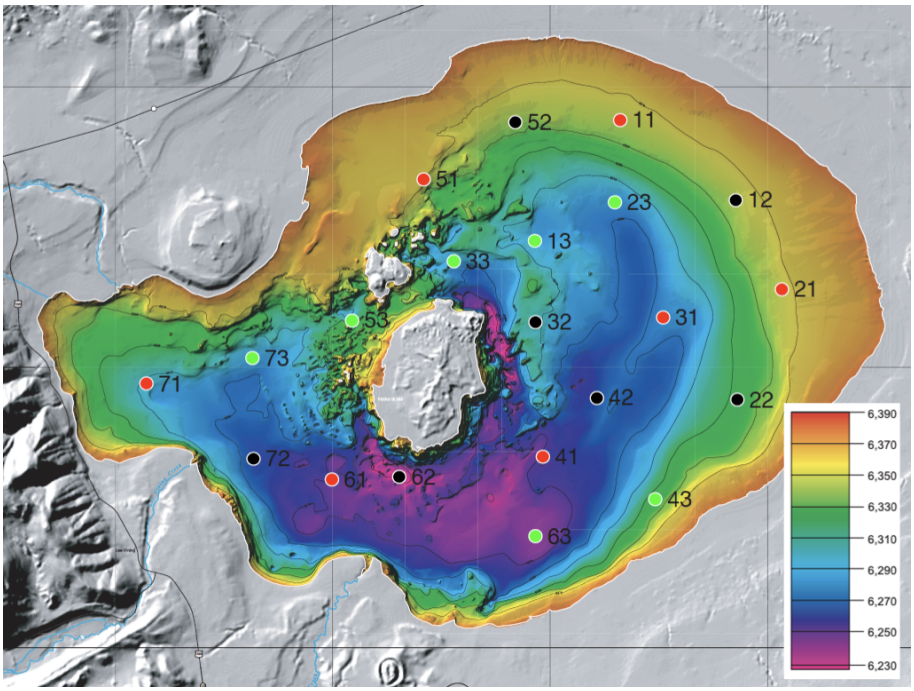

Figure 2.3: Bathymetric profile of Mono Lake in feet above sea-level with the lake-bottom station locations. The first number denotes the instrument number and the color of the station marker and second digit denotes which deployment. Modified from Constable and Peacock [2018]. Bathymetry from [Raumann et al., 2002].

With motivation from preliminary findings presented in Constable and Peacock [2018] from the lake-bottom data, Scripps scientists and the USGS returned to collect another data set on land north of Mono Lake in October 2018. These sites were collected with Zonge Electromagnetic Network (ZEN) High-Res Receiver™, which uses a 32-bit analog digital converter (ADC) and a broadband, 6-channel receiver to record time series data. For this survey four instruments were deployed and left overnight, then recovered and moved five times for a total of 24 stations. The instruments recorded at 256 Hz sampling frequency for 8-hour windows, interrupted in between by 10 minutes sampling at 4096 Hz. A remote magnetic reference recorded continuously at the same location as the Mono Lake surveys in 2017, shown in Figure 2.9. Additionally, Conductivity - Temperature - Depth soundings were taken in the lake at 7 different locations.

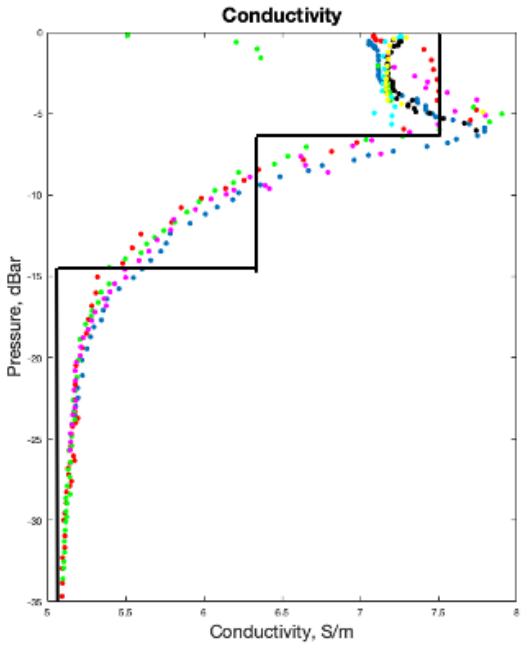

Figure 2.4: CTD soundings were taken at 7 sites in Mono Lake during the 2017 survey. Three distinct layers of lake water were derived from this.

2.3 Data Processing

2.3.1 Data Modifications

The data north of the lake were processed along with the remote reference data using a multi-station processing code. In order to do this, the Zonge data had to be reformatted into an identical file that is outputted by the Scripps instrument used to record the remote reference. The data north of the lake were also processed by Jared Peacock at the USGS using a single-station method.

The Zonge instruments create a binary file specific to the instrument in a *Z3D* format, which consists of headers and 32-bit data in counts and 32-bit timestamps in GPS time. Alternatively, the binary files produced from Scripps instruments contain a 512-byte header, a directory and 512-byte data blocks consisting of a 14-byte header

and 166 24-bit data points and timestamps in UTC time. In order to process the Zonge data with the data collected at the remote reference site, the Zonge files were read into Matlab and written back out into a Scripps format.

Since the remote station was collected using Scripps instruments at 1000 Hz, the data had to be downsampled in Matlab from sampling rate to 256 Hz, which results in a reduction of resolution. The *resample* function in Matlab applies a lowpass filter to the data and interpolates. The land data used a different magnetometer sensor (supplied by Zonge) than the remote station, which used a pair of BF-4 induction coils and this difference was reflected in the calibration files. Additionally, a factor of 16 was divided out of the 32-bit data in order for them to be written out in 24-bit format, however this factor was added back into the conversion factor later in the processing.

2.3.2 Multi-station processing

The goal of the multi-station processing technique is to improve the signal-to-noise ratio by removing any bias and coherent noise present in a single station's recording [Egbert, 1997]. The processing uses two steps, *dnff* and *multmtrn* to arrive at apparent resistivity and phase values that can be used in inversion. *dnff* is the initial step that transforms time series data into the frequency domain. This is done using overlapping fast Fourier Transform (FFT) windows and cascade decimation, creating Fourier coefficient estimates along with uncertainties at each frequency. The FFT breaks the time series into windows, calculates the coefficients, then averages them. Using eight specified decimation windows, this process is repeated. The data are also corrected based on instrument calibrations. *multmtrn* uses the Fourier coefficient estimates to calculate complex transfer functions. A robust errors-in-variables (RMEV) approach is used for eigenvalue analysis in determining whether the plane wave approximation is correct, which accounts for noise in all channels. The user specifies groups of stations in the

same deployment and the overlapping time windows are used to find coherence in the data. The remote reference station containing a continuous recording of the magnetic field in the x and y directions is included in each group with the data.

The approach used was to process all sites at once in the same deployment along with the remote station, and then identify the noisier sites and remove them from the group. This allows the stations with higher quality to be reprocessed without the bias from the noisier stations. The hope is that the noisy stations are cleaned up in the initial grouping.

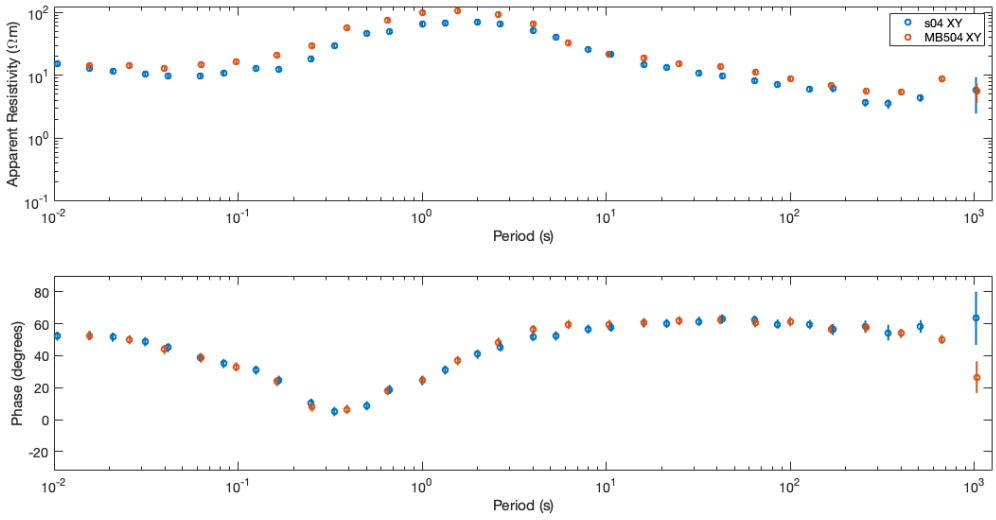

Figure 2.5: A comparison of MT data processed using the multi-station approach (s04) and conventional single-station processing (MB504). Shown in this plot is just the TE mode for one land station collected on the north side of the lake. Note that the data were processed at difference frequencies.

The two processing methods were compared for the stations north of the lake. The single-station processing shows a bias in the apparent resistivities but the phases are almost identical. Some variance is seen between the two processing methods at the longer periods. These data are relatively clean and the multi-station processing may show more benefit in noisier data, so more work is needed.

2.4 Lake Bottom Data Propagation

In the 1D case, the MT impedance value that is measured on the seafloor is not affected by the conductive seawater above it [Constable et al., 1998]. This same principle applies to lake bottom data. For 2D modeling in MARE2DEM, the receivers can be placed on the lake floor and the overlying water can be put into the model. However, for 3D modeling, limitations in the publicly available codes prevents the inclusion of bathymetry, so the receivers must be modeled at the surface.

Modeling the station locations at the lake surface renders a distortion from the underlying lake water and must be accounted for in the data. 2D forward modeling in MARE2DEM illustrates the difference between MT responses on the lake surface and on the lake bed, caused by the effects of the conductive lake water.

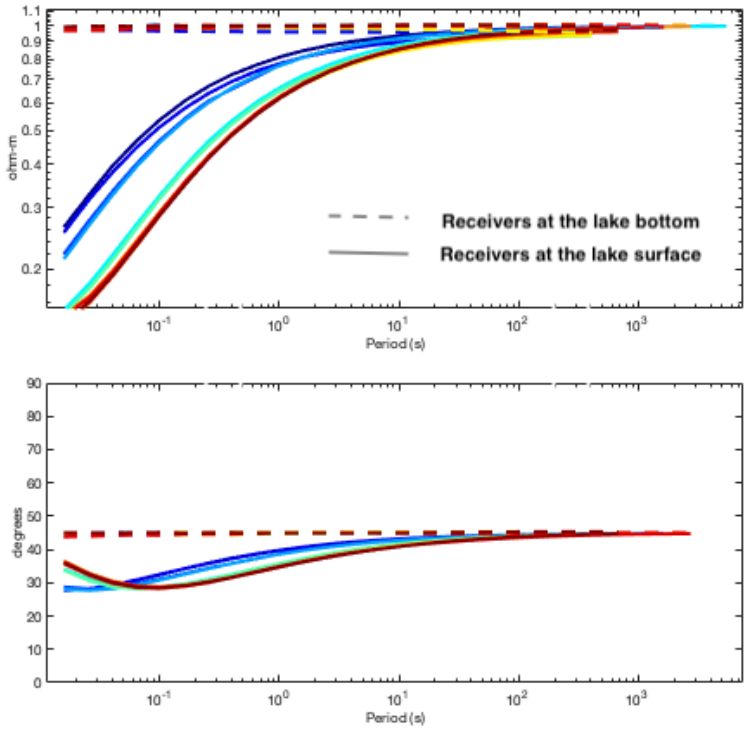

Figure 2.6: 2D forward models for a uniform 1 Ω-m halfspace underlaying the three layers of Mono Lake, derived from CTD measurements shown in Figure 2.4. The broken lines are the result with the receivers at the lake surface and the solid lines are the stations at their correct depth on the lake bottom. The colors represent different stations in the lake, which are located at varying depths. The difference in this "lake effect" is due to the amount of water above the station. The slight difference in apparent resistivities for the broken lines shows the difference between a 1D and 2D approximation - the 2D effect of the edge of lake is apparent.

As shown in Figure 2.6, the effect is more prominent at shorter periods, which is attributed to the fact that higher frequencies equate to a shallower depth of penetration, so the sensitivity to the lake water increases as the period shortens.

Using the 1D recursion relation, the lake bottom data can be propagated to the top of the lake. The recursion relation in Section 2.1.1 relates the impedance at the top of a layer with the impedance of the layer below it with resistivity ρ and thickness h. Recalling Equation 2.16,

$$\hat{Z}_n = Z_n \frac{\hat{Z}_{n+1} + Z_n tanh(ik_n h_n)}{Z_n + \hat{Z}_{n+1} tanh(ik_n h_n)}$$

the starting value for Z_{n+1} will be the impedance that is measured on the lake-bottom. The complex wavenumber k and the instrinsic impedance Z_n are a functions of the resistivity of the layer. For the case of the lake bottom propagation, the resistivity layers correspond to layers of lake water, as shown in Figure 2.4.

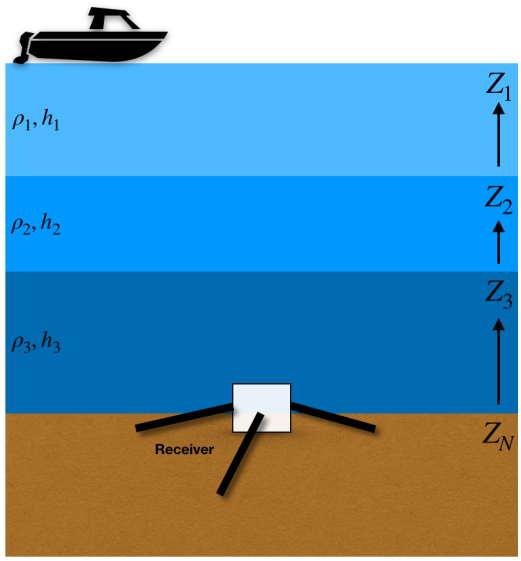

Figure 2.7: Diagram of a layered lake with impedance $Z_1, ..., Z_N$.

The CTD measurements were used to create a simpler three-layer model for the lake water, with 7.25 S/m, 5.99 S/m and 5 S/m at 7 meters, 8 meters, and 15 - 26 meters thickness, respectively, from the top of the lake. The bottom layer thickness depends on the location of the station, as the lake bottom is around 30 to 45 meters at different stations.

The data were propagated upwards using the recursion relation using Matlab. The script reads in the apparent resistivity and phase values from the data file, converts them to impedance and then iterates through every layer until the data are modeled at the surface rather than at the depth at which it was recorded. Using this final impedance value, the data are then converted back to apparent resistivity and phase for use in a 3D inversion.

This approach was validated using 2D forward models, showing that the 2D effects were did not have a significant impact on the 1D assumptions used in the propagation scheme. Testing showed that the 2D effects were smaller when the data are rotated before propagation, rather than propagating in instrument coordinates and rotating afterwards. A similar 2D inversion was ran as explained below in Section 2.5, where the lake-bottom data were inverted, but with the receivers on the surface of the lake in the model by using the upward continued data in place of the lake bottom. The two results show only slight differences which validates the upward propagation approach.

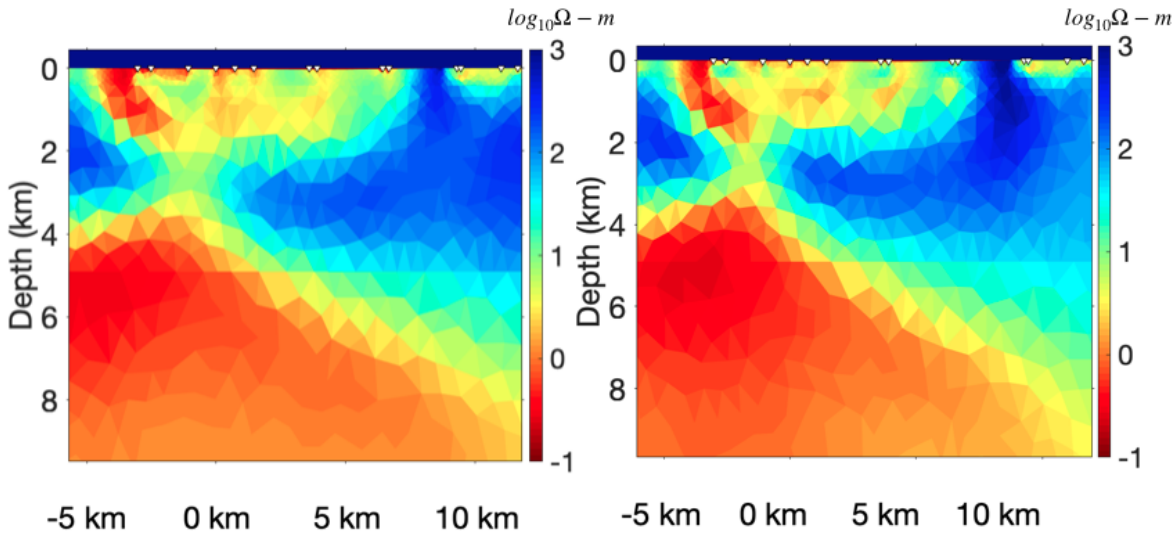

Figure 2.8: 2D inversion model obtained from lake bottom data (left) compared with an inversion run using propagated lake data and receivers on the surface of the lake in the model (right), showing that the upward continuation of the data gives a very similar result.

2.5 Inversion

2.5.1 2D Inversion

2D Inverse modeling of the data was done using MARE2DEM (Modeling for Adaptively Refined Elements for 2D Electromagnetics), an open-source program that can handle MT or controlled-source electromagnetic (CSEM) data in land or marine settings [Key, 2016]. MARE2DEM is a parallel adaptive finite-element code that carries out non-linear inverse calculations using the Occam inversion method, which seeks a smooth model to fit the data within a target tolerance [Constable et al., 1987]. The goal of Occam inversion is to minimize the functional U.

$$U = |\mathbf{Rm}|^2 + |\mathbf{P}(\mathbf{m} - \mathbf{m}_*)|^2 + \mu^{-1}[|\mathbf{W}(\mathbf{d} - F(\mathbf{m}))|^2 - \chi_*^2] \tag{2.19}$$

where $\mathbf{R}$ = differencing operator

$\mathbf{m}$ = model vector containing $\log_{10}\rho$

$\mathbf{P}$ = scaling parameter

$\mathbf{m}_*$ = a priori preference model

$\mathbf{W}$ = diagonal weight matrix

$\mathbf{F(m)}$ = forward model response $\mathbf{m}$

$\mathbf{d}$ = EM or MT data

μ = Lagrange multiplier

χ_*^2= target misfit

Mamba 2D, a model building assistant, allows the user to create a model with prior geologic, bathymetric and topographic knowledge. χ_*^2 is specified by the user in the input files and the code iterates through multiple models until it finds the smoothest model within a target root mean square (RMS) value, which for a set of discrete data

misfit values (x_1,...x_n) , or the difference between the data and forward model F(m), is calculated through Equation 2.20.

$$x_{RMS} = \sqrt{\frac{\chi_*^2}{n}} = \sqrt{\frac{x_1^2 + x_2^2 + ... + x_n^2}{n}} \tag{2.20}$$

Two parallel profiles at 135° were selected for inversion, shown as A-A' and B-B' in Figure 2.9, consisting of land and lake-bottom data. The two data types were processed at different frequencies due to differing sampling frequencies, so the data were interpolated to the same frequencies in order to decrease processing speeds. The data were rotated in-line and the previously processed data collected south of the lake were interpolated to frequencies that corresponded to the data collected on the lake bottom. The southern land data were collected a few years prior and original (single-station) processing was used for this set. The TE resistivities for the land data were excluded in the 2D inversions due to their sensitivity to 3D geologic structure. The starting model for both profiles was a 1 Ω-m halfspace model that included the bathymetry of the lake along the lake water profile with three resistivity layers, 0.2 Ω-m, 0.167 Ω-m and 0.138 Ω-m bottom to top, which again were derived from the CTD measurements shown in Figure 2.4. The inversions ran to a local 12-core desktop, but can also be run on a cluster. Results are discussed in Section 3.1.

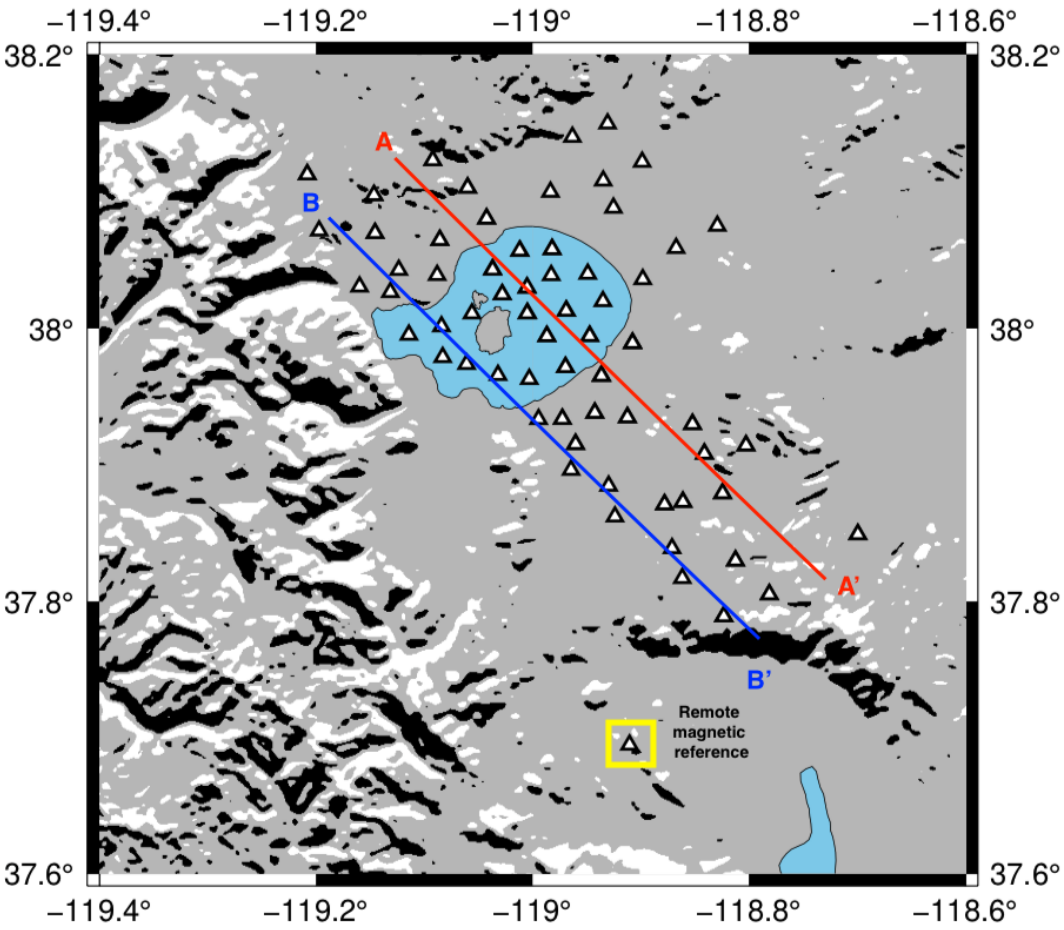

Figure 2.9: Map of the station locations for the 2017 lake-bottom survey and the 2018 land survey. The sites previously collected by the USGS that were used for inversion are also included. Profiles A-A' and B-B' were chosen for inversion along the line of strike, which is well defined at 135° [Constable and Peacock, 2018]. The remote reference station used for processing is located south of the lake. The stations south of Mono Lake were processed by the USGS.

2.5.2 3D Inversion

A 3D inversion was ran using ModEM, incorporating the lake-bottom data, the 2018 land data, and the previously collected land data south of the lake. This code does not allow bathymetry in the model, so the lake data were propagated to the lake surface as previously described. The data were interpolated to the same 23 frequencies ranging from .0059 to 57.9203 Hz. The inversion was run by Jared Peacock using the USGS

Yeti Supercomputer and began with a 100 Ω-m halfspace that included the lake as an a priori conductive body in the starting model.

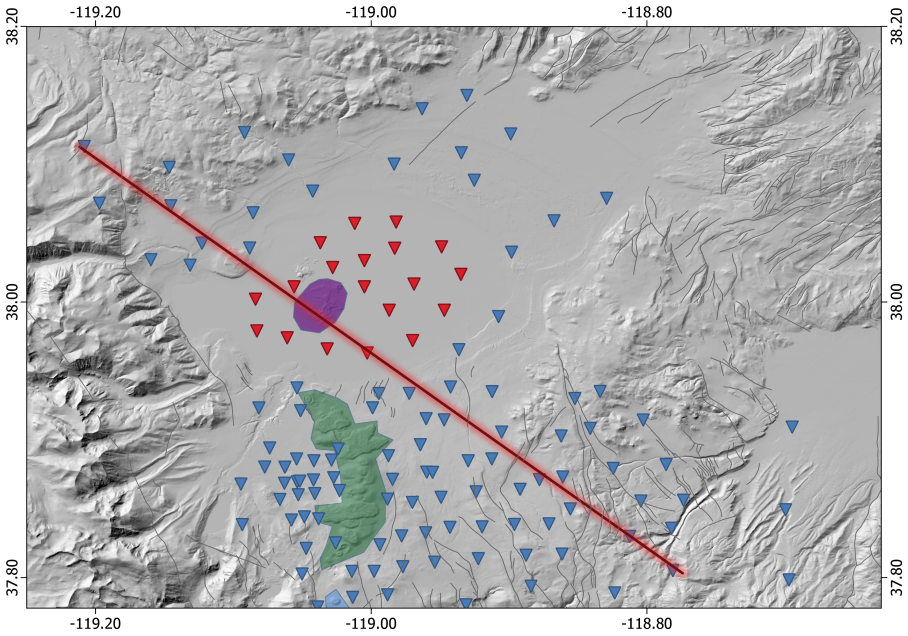

Figure 2.10: Basemap of the stations used in 3D inversion. The purple and green regions represent Mono Craters. The sites in blue are land sites, while the sites in red are in the lake. The sites south of the lake were collected by the USGS in 2015. The red indicates the 2D slice shown in Figure 3.6. Map courtesy Jared Peacock.

Chapter 3

Results and Discussion

This chapter presents the results of the 2D inversion as well as a discussion of the geologic interpretation and a comparison to previous geologic, geophysical and geochemical findings in this area. The preliminary 3D inversion result is also discussed.

3.1 2D Inversion

The data were inverted along two parallel profiles along the line of strike at 135°, as shown in Figure 2.9. The inversions have a resolvable depth of about 40 km. The two results show clear differences as one moves laterally, but have similar features. The large conductive body from about 5 to 25 km depth appears in both models, with a value of about 0.1 Ω-m. The anomaly seems to have a more prominent extent to the northwest side in Profile A, which could mean that the conductor extends to the north of the lake. The initial interpretation of this conductor is magma or a hydrothermal reservoir, underlaying hydrothermal fluids 1-5 km directly below Mono Lake that come up to the surface as hot springs. In Profile A there is also a conductive feature (around 1-2 Ω-m) to the southeast of the lake that does not appear in Profile B and is possibly another smaller hydrothermal body.

Seismic refraction studies by Hill et al. [1985] concluded that the depth to basement in Mono Basin is 1-2 km, which is in good agreement with model A. The near-surface sediments are composed mostly of debris from surrounding structure such as the Sierra Nevada as well as past volcanic eruptions. According to Bailey [1989a], the prevolcanic

basement of the Inyo-Mono crater chain area is mostly granitic rock of the Sierra Nevada batholith, which is in agreement with the higher resistivities to the south of the lake. The literature values for granite resistivity range up to 10^4 Ω-m, however the porosity from fractures may explain the lower value of 10 to 100 Ω-m. It is also important to note that the basement contains graphite, which is very conductive.

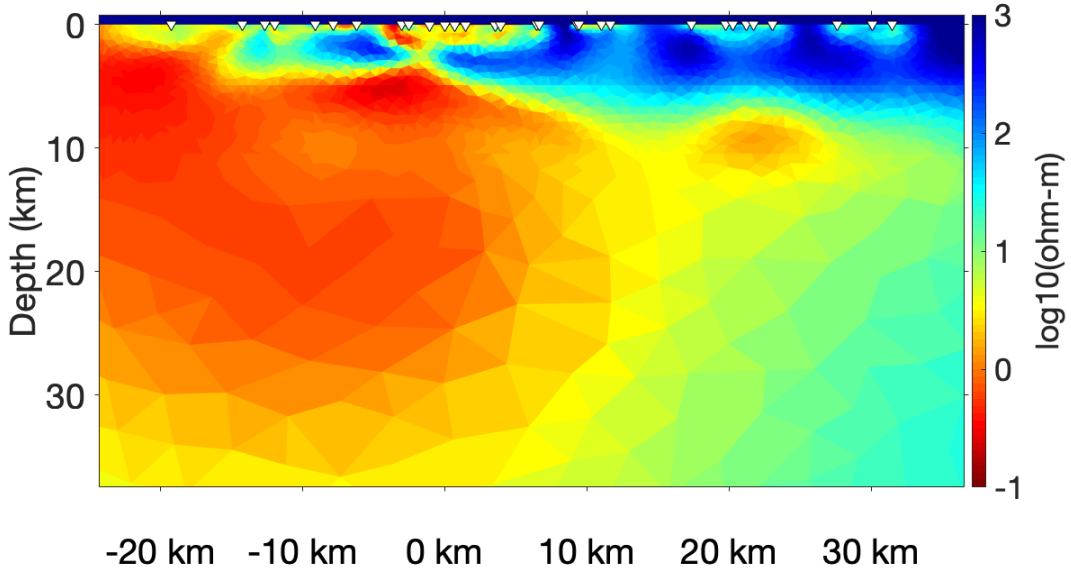

(a) Profile A, RMS=1.24

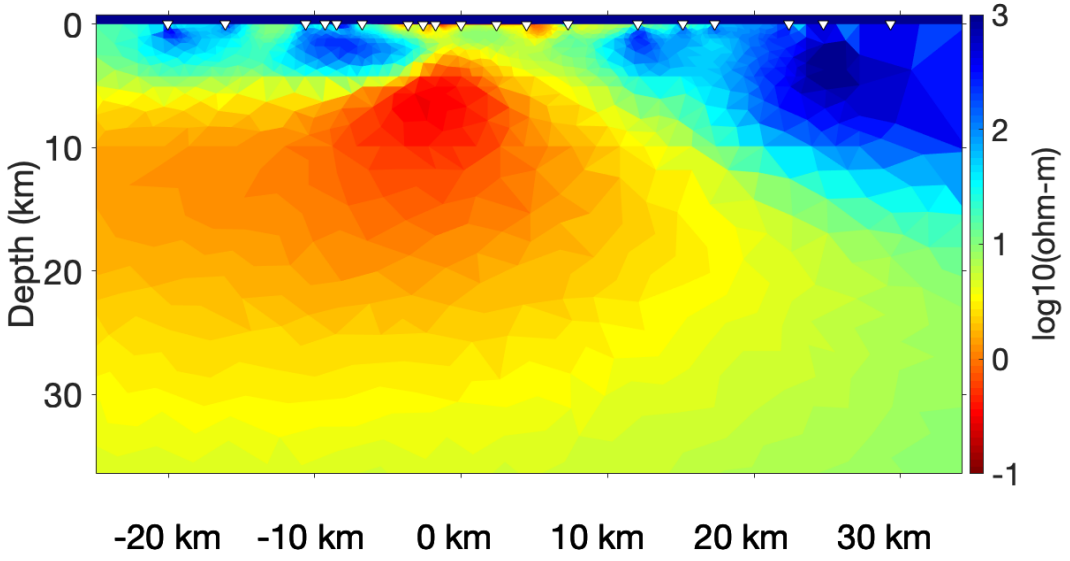

(b) Profile B, RMS=2.29

Figure 3.1: The 2D inversion results for the two profiles shown in 2.9. Both profiles have considerably good data fits. Mono Lake is centered at 0 km on both profiles.

3.2 Interpretation

3.2.1 Partial Melt Estimates

Partial melt is determined by the behaviour of a rock containing different minerals that have varying melting temperatures. Equation 3.1 is used to describe the relationship between the electrical conductivity (σ), water content (w), pressure (P) and temperature (T) for andesitic rock [Guo et al., 2017], which is an intermediate between basalt and rhyolite, containing 57% to 63% SiO_2 [R. W. Le Maitre and Woolley, 2002].

$$log\sigma = 5.23 - 0.56w^{0.6} - \frac{8130.4 - 1462.7w^{0.6} + (581.3 - 12.7w^2)P}{T} \tag{3.1}$$

Estimates of the melt resistivity can be made as a function of different temperatures and water contents, as shown Figure 3.2a. Using the conductivity values from Equation 3.1 the bulk conductivity (σ) is calculated using the Hashin-Shtrikman upper bound (HS+), which models a fully connected conducive phase [Ni et al., 2011]. Equation 3.2 gives the bulk conductivity as a function of the individual conductivities and volume fractions.

$$\sigma = \sigma_2 \left[1 - \frac{3F_1(\sigma_2 - \sigma_1)}{3\sigma_2 - F_2(\sigma_2 - \sigma_1)}\right] \tag{3.2}$$

where σ_1 is the conductivity of the solid mantle and σ_2 is melt conductivity calculated in Equation 3.1. The conductivity of the solid mantle near the melting point is set to 0.1 S/m, F_2 is the volume fraction of the melt and F_1 is the volume fraction of the solid mantle, equal to $1 - F_2$.

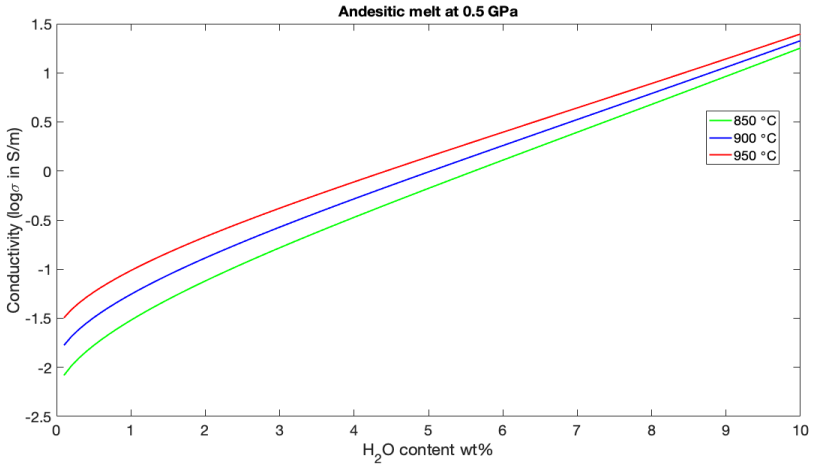

(a)

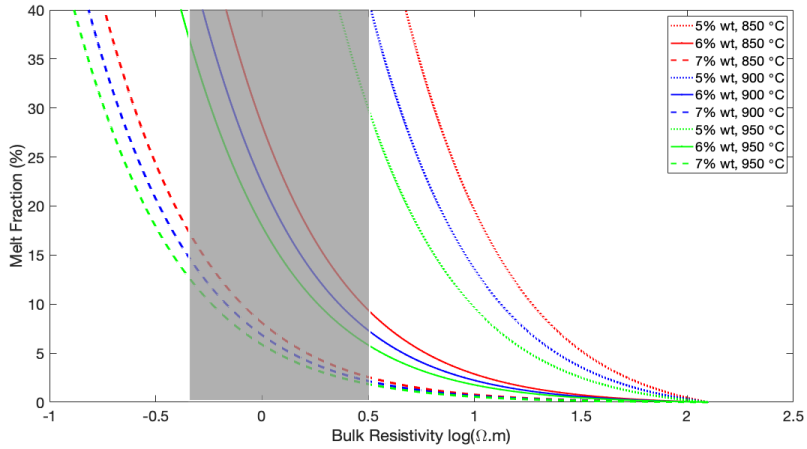

(b)

Figure 3.2: (a) Estimates of melt resistivity at 0.5 GPa, calculated using Equation 3.1 for temperatures 850°C, 900 °C and 950°C. The equation is evaluated at water contents of 0 to 10%. (b) Bulk resistivity as a function of melt fraction for water contents 5-7% and temperatures 850°C, 900°C, 950°C.

The 2D model indicates that the bulk conductivity in regions of melt is about 0.5 - 3 Ω-m for the large conductor from about 5 - 10 km depth. Using the estimates in Figure 3.2b, the range of melt fraction is shown in the grey box. Water content of 5 wt% can almost be ignored because it mostly doesn't lie in the respective range of resistivities. The range is anywhere from 5-40% melt assuming that the water is 6% wt. The difference in the three temperatures is minimal.

3.2.2 Earthquakes and Geologic Features

The inversion model is in good agreement with previously mapped geologic features. Regional faults that have been mapped at the surface are overlain onto a shallow section of Profile A, shown in Figure 3.3. The fault at 0 km is likely allowing fluid flow below Mono Lake, contributing to the large conductive zone in the top 0 to 3 km. There are also various volcanic vents and thermal springs that have been observed in the area that align with areas of higher conductivity.

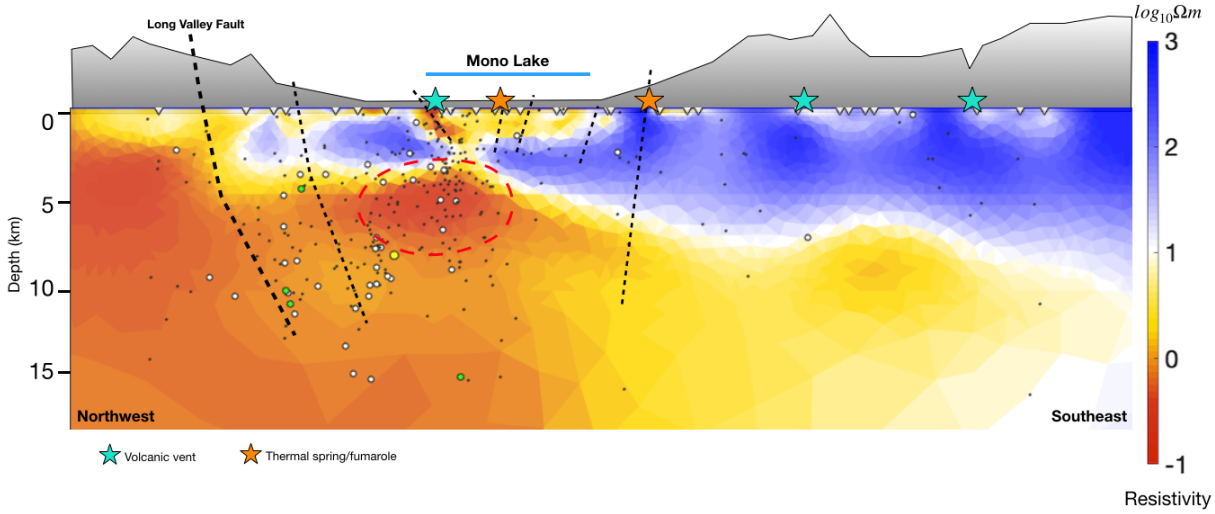

Figure 3.3: Geologic features such as volcanic vents, fumaroles and thermal springs along Profile A. The dashed lines are regional faults. The conductive feature in question is outlined in red.

In combination with MT inversion results, earthquake locations can be useful to interpret the brittle-ductile transition and faulting. The earthquake depths and locations were taken the from Northern California Earthquake Catalog Search provided by the Berkeley Seismology Lab, which includes all events from 1967 to present. Epicenters of earthquakes with magnitude 1.0 and higher within 5 km of the line were plotted on each Profile, shown in Figure 3.4. A majority of the events occur in the upper 15 km, which can be inferred as the brittle-ductile transition. The transition zone is where increasing

brittle strength with depth is equal to the upwards increasing ductile strength, making it the strongest part of the crust and susceptible to earthquakes.

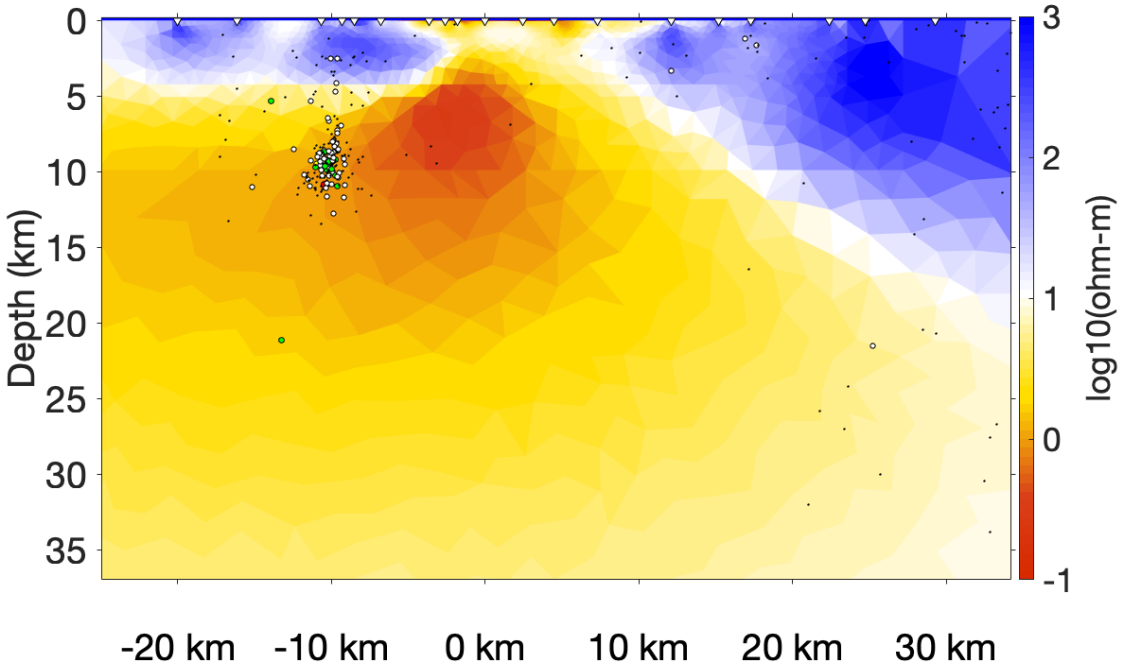

Figure 3.4: Earthquake epicenters from 1967 to present plotted on Profile B. The color of the marker denotes the magnitude of the events.
Black: 1.0 - 1.9, White: 2.0 - 2.9, Green: 3 - 3.9, Yellow: 4 - 4.9, Red: 5.0+

3.3 3D Inversion

The 3D inversion result shows a similar conductor located directly under Mono Lake as well as a deeper conductor (15-30 km) that extends from a few kilometers north of the lake to about 30 km to the southwest. The resistivity values are slightly higher in the 3D model (10-20 Ω-m), likely due to smoothing as the starting model is 100 Ω-m. The very conductive lake could also render an effect on the resistivity of everything beneath it. An interesting feature to note is the shallow conductor to the north of the lake, which could be hydrothermal fluids or melt. As shown in Figure 3.6, the earthquakes around this feature are prolific.

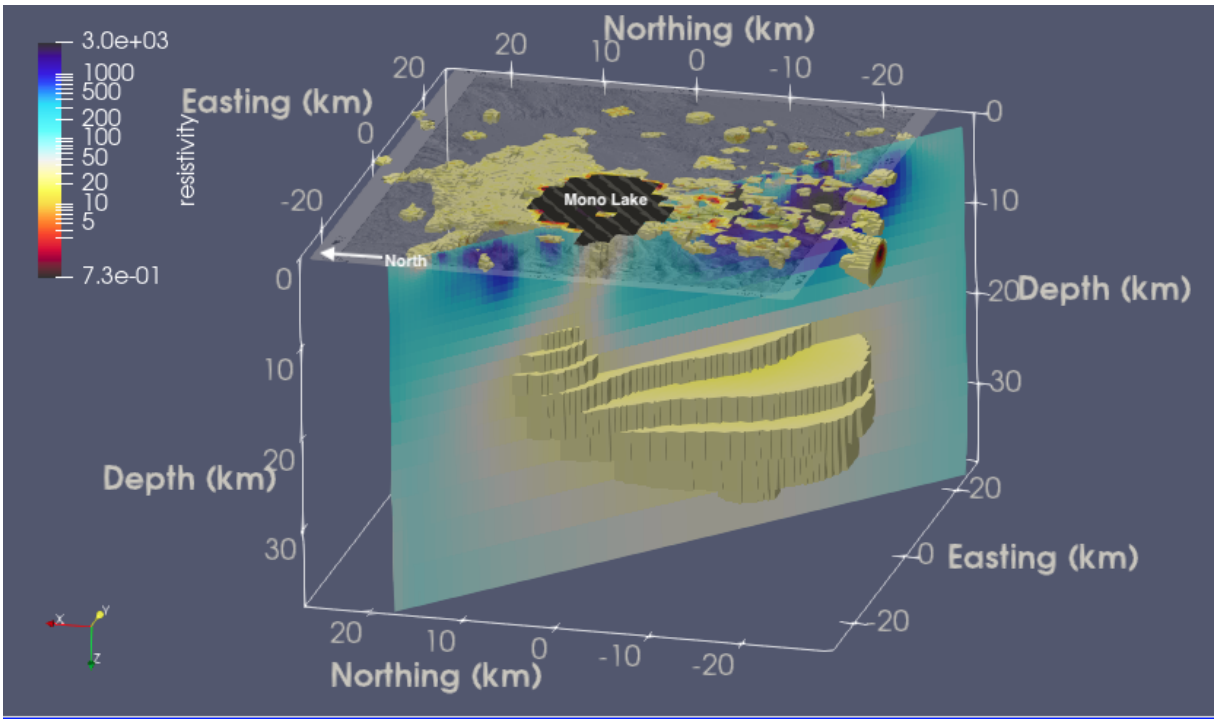

Figure 3.5: 3D inversion showing the extent of the deeper conductor under the lake and extending to the southeast using an isosurface (about 20 Ω-m). The same behavior is seen in the 2D result, Figure 3.1a, with the shallower conductors connecting to the deeper features.

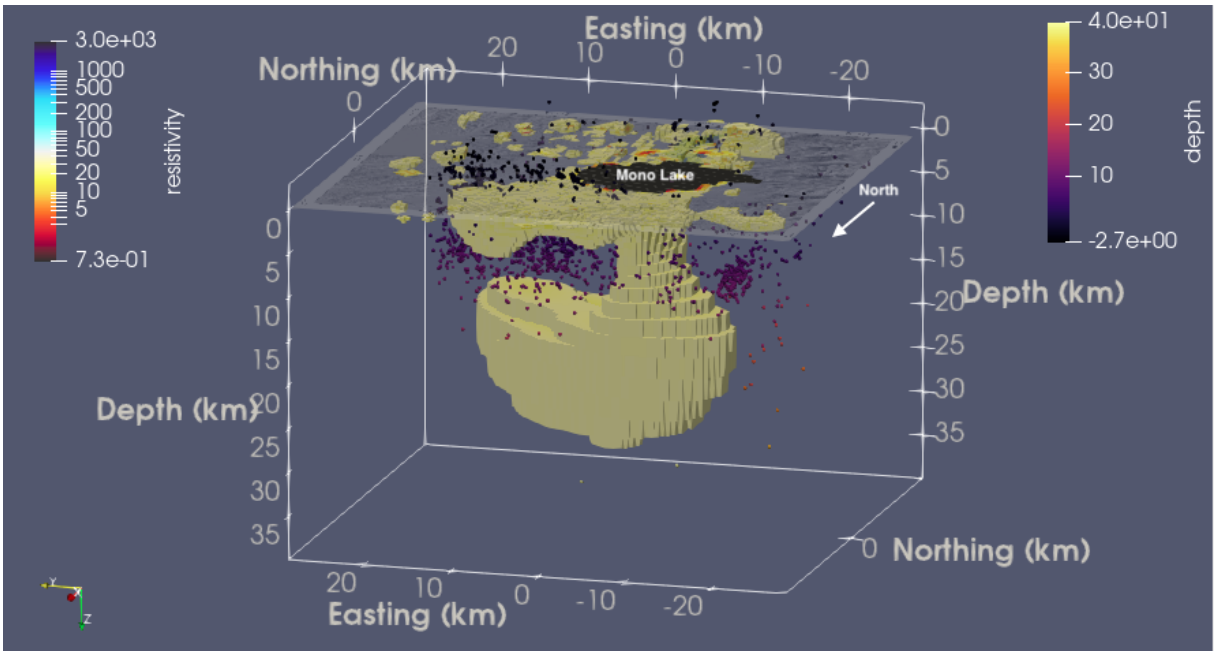

Figure 3.6: A second of the 3D result with earthquake epicenters plotted. The color of the earthquake point represents the depth.

Chapter 4

Conclusions

The land and lake-bottom MT data sets were combined successfully with existing MT data to study the Mono Basin area. In compilation with results from previous studies, useful assumptions can be made about the past and future volcanism. The 2D and 3D inversion results show a large conductor several kilometers under Mono Lake extending to the north of the lake, at least by a few kilometers. They also clearly show a hydrothermal system directly under the lake, that is possibly being fed by the deeper source through a regional fault. The 3D results show a shallow conductor extending several kilometers north of the lake; this along with the extensive seismic activity aligned with the feature suggests recent volcanic activity.

The young age of the Inyo-Mono Craters themselves suggest that the cycle of eruptions has not ended. Although more information (possibly time-dependent) is needed, some suggestions can be made about the nature of future eruptions in the Long Valley-Mono Basin system from these results. Considering the conductor identified under Mono Basin and north it is likely that the eruptions will follow the preexisting northward progression. Nixon [2012] suggests that the next eruption will likely be explosive and rhyolitic, judging by the most recent eruptions record. However, the presence of hydrothermal fluids may suggest that this eruption could be driven by steam

The investigation of this area is by no means complete. Future work would include the combined interpretation of this data with seismic or gravity data, providing additional information on such as subsurface fault structure and fluid flow. Deploying more MT stations to the north of this data set could distinguish the conductors that

extend past the limit of the data set towards the Bodie Mountains.

References

R.A. Bailey. Geologic map of long valley caldera, mono-inyo craters volcanic chain and vicinity, eastern california. *US Geological Survey*, pages 637–650, 1989a.

Roy Bailey. *Simplied Geologic Map of Long Valley Area with inset map*, 1989b.

Marcus Bursik and Kerry Sieh. Range front faulting and volcanism in the mono basin, eastern california. *Journal of Geophysical Research*, 94:15,587–15609, 11 1986.

Louis Cagniard. Basic theory of the magnetotelluric method of geophysical prospecting. *Geophysics*, 18(3):605–635, 1953.

Steven Constable and Jared Peacock. Marine em on land: Mt measurements in mono lake. EM Induction Workshop, 8 2018. EMIW workshop abstract.

Steven C. Constable, Robert L. Parker, and Catherine G. Constable. Occam's inversion: A practical algorithm for generating smooth models from electromagnetic sounding data. *Geophysics*, 52(3):289–300, 03 1987.

Steven C. Constable, Arnold S. Orange, G. Michael Hoversten, and H. Frank Morrison. Marine magnetotellurics for petroleum exploration part i: A sea-floor equipment system. *Geophysics*, 63(3):816–825, 1998.

Gary D. Egbert. Robust multiple-station magnetotelluric data processing. *Geophysical Journal International*, 130(2):475–496, 08 1997. ISSN 0956-540X.

C. M. Gilbert, M. N. Christensen, Yehya Al-Rawi, and K. R. Lajoie. Structural and Volcanic History of Mono Basin, California-Nevada. In *Studies in Volcanology*. Geological Society of America, 01 1968. ISBN 9780813711164.

Xuan Guo, Bin Li, Huaiwei Ni, and Zhu Mao. Electrical conductivity of hydrous andesitic melts pertinent to subduction zones. *Journal of Geophysical Research: Solid Earth*, 122(3):1777–1788, 2017.

David P. Hill, E. Kissling, J. H. Luetgert, and U. Kradolfer. Constraints on the upper crustal structure of the long valley-mono craters volcanic complex, eastern california, from seismic refraction measurements. *Journal of Geophysical Research: Solid Earth*, 90(B13):11135–11150, 1985.

Kerry Key. Mare2dem: a 2-d inversion code for controlled-source electromagnetic and magnetotelluric data. *Geophysical Journal International*, 207(1):571–588, 08 2016.

Huaiwei Ni, Hans Keppler, and Harald Behrens. Electrical conductivity of hydrous basaltic melts: Implications for partial melting in the upper mantle. *Contributions to Mineralogy and Petrology*, 162:637–650, 09 2011.

Elizabeth Nixon. Geologic history of the mono basin. pages 1–11, 2012.

L.C. Pakiser, M.F. Kane, and W.H. Jackson. Electrical conductivity of hydrous basaltic melts: Implications for partial melting in the upper mantle. *Contributions to Mineralogy and Petrology*, 162:637–650, 09 1964.

J. R. Peacock, M. T. Mangan, D. McPhee, and D. A. Ponce. Imaging the magmatic system of mono basin, california, with magnetotellurics in three dimensions. *Journal of Geophysical Research: Solid Earth*, 120(11):7273–7289, 2015.

B. Zanettin M. J. Le Bas B. Bonin P. Bateman G. Bellieni A. Dudek S. Efremova J. Keller J. Lamere P. A. Sabine R. Schmid H. Sorensen R. W. Le Maitre, A. Streckeisen and A. R. Woolley. *Igneous Rocks: A Classification and Glossary of Terms*. Cambridge University Press, 2002.

Christian G. Raumann, Scott Stine, Alexander Evans, and Jerry Wilson. Digital bathymetric model of mono lake, california. https://pubs.usgs.gov/mf/2002/2393/, 2002.

Brian R. Spies. Depth of investigation in electromagnetic sounding methods. *Geophysics*, 54(7):872–888, 1989.

Stanley H. Ward and Gerald W. Hohmann. *4. Electromagnetic Theory for Geophysical Applications*, pages 130–311. Society of Exploration Geophysicists, 2020/04/10 1988. ISBN 978-0-931830-51-8. doi: doi:10.1190/1.9781560802631.ch4.

Appendix

5.1 Data Fits

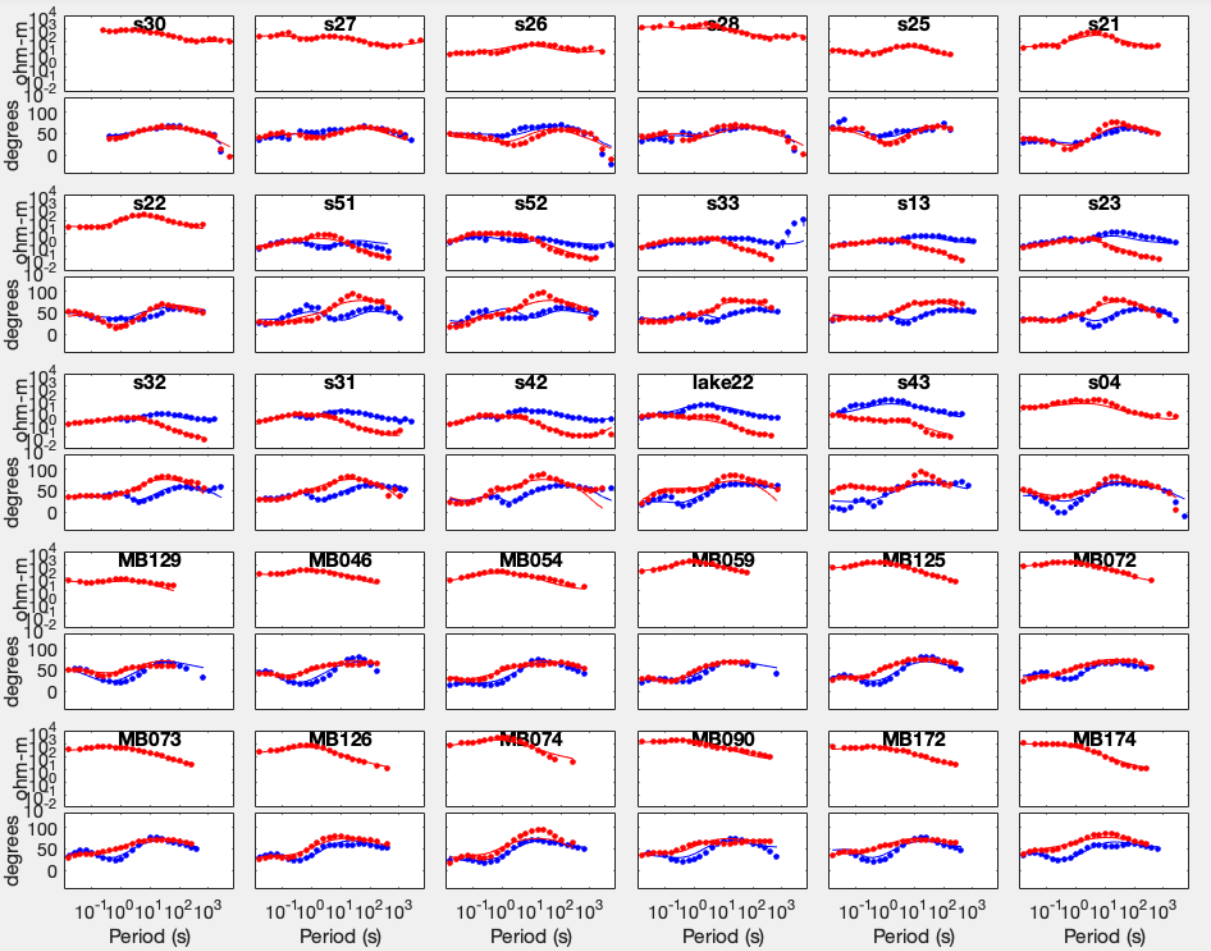

Figure 5.1: The fits for the 2D MT data. Note that for the land sites, the TE resistivities are removed.

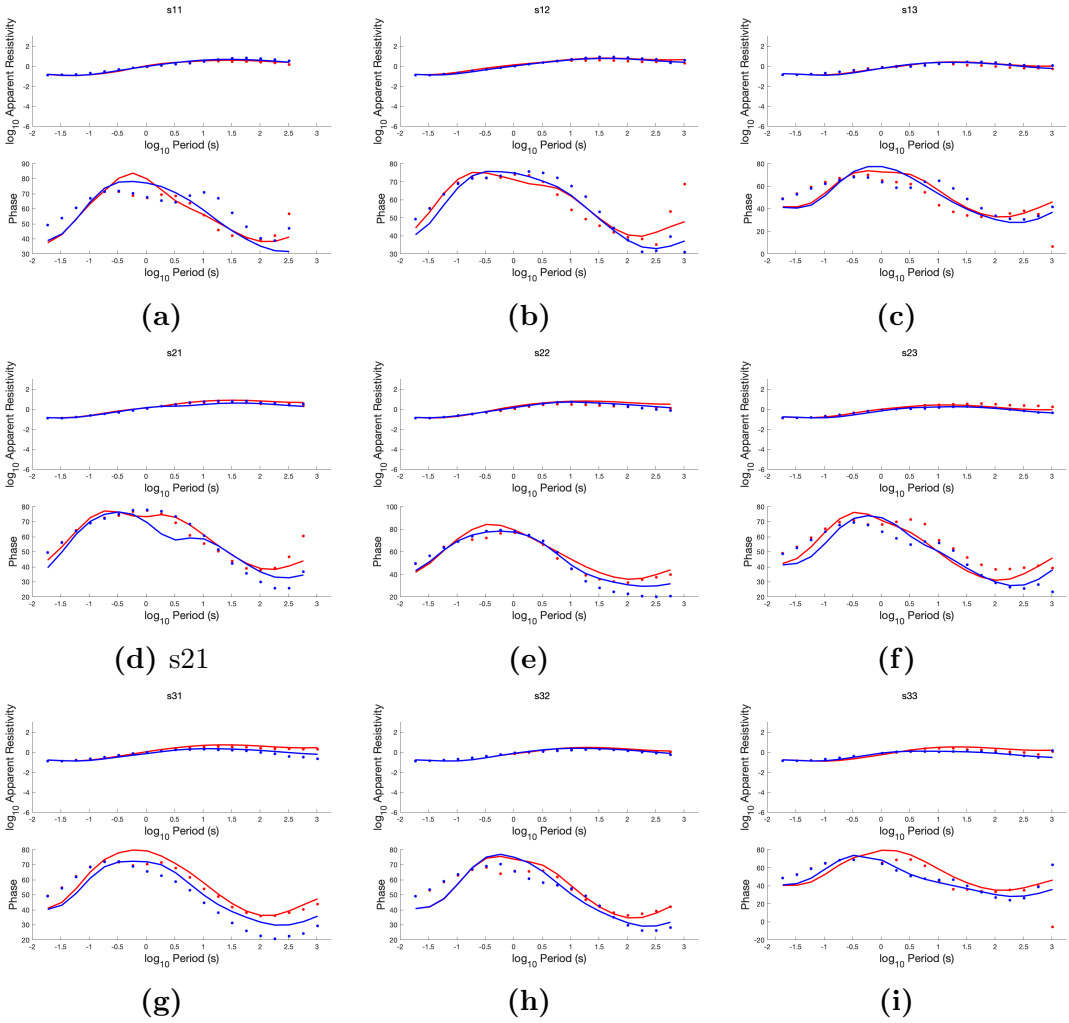

Figure 5.2: 3D data fits for the lake stations.

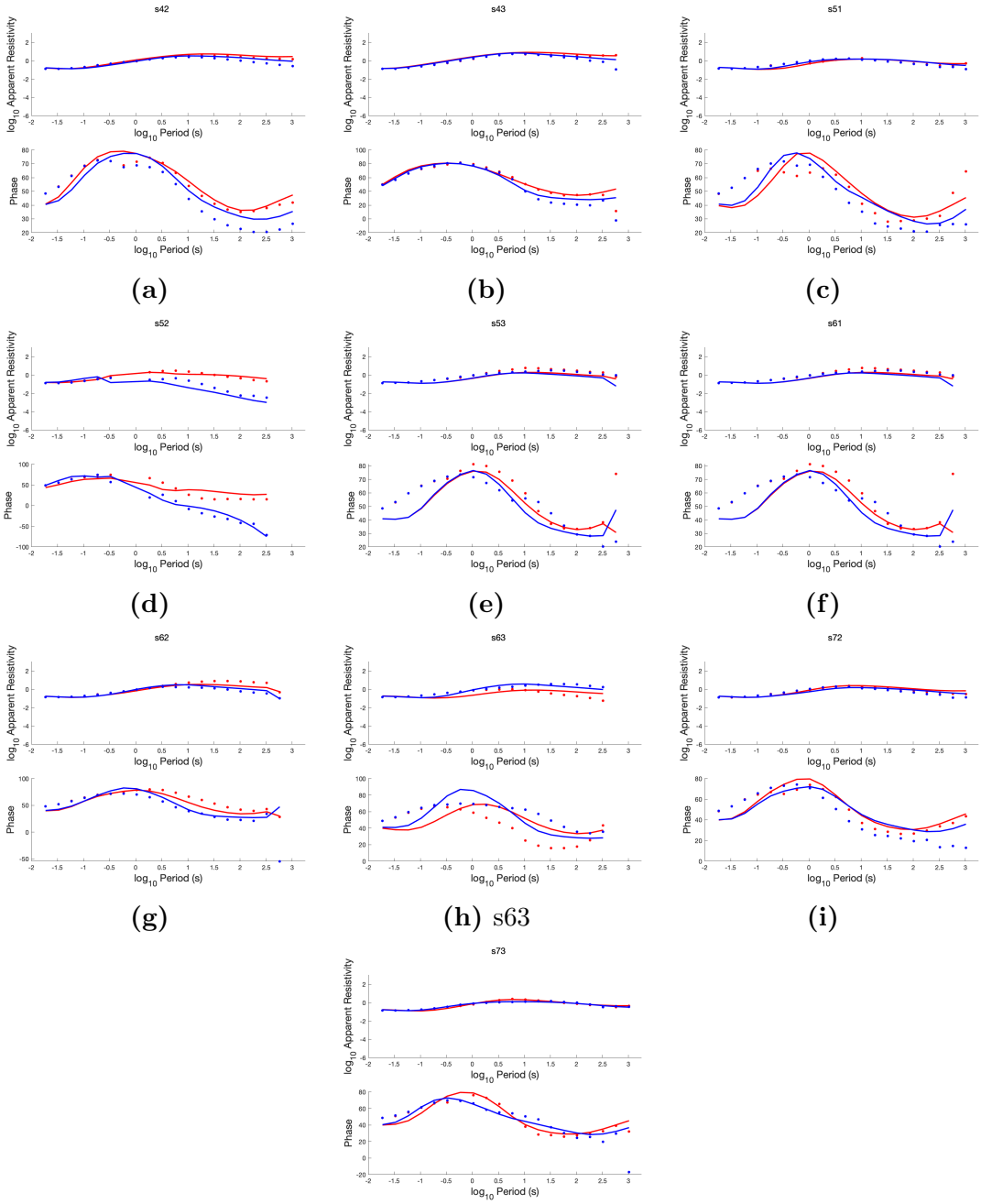

(a) **(b)** **(c)**

(d) **(e)** **(f)**

(g) **(h)** s63 **(i)**

(j)

Figure 5.3: 3D data fits (continued).